



Contents lists available at ScienceDirect

Science Bulletin

journal homepage: www.elsevier.com/locate/scib

Article

Light-emitting field-effect transistors with EQE over 20% enabled by a dielectric-quantum dots-dielectric sandwich structure

Lingmei Kong^a, Jialong Wu^a, Yunguo Li^b, Fan Cao^a, Feijiu Wang^{c,*}, Qianqian Wu^a, Piaoyang Shen^a, Chengxi Zhang^a, Yun Luo^a, Lin Wang^a, Lyudmila Turyanska^d, Xingwei Ding^{a,*}, Jianhua Zhang^a, Yongbiao Zhao^e, Xuyong Yang^{a,*}

^a Key Laboratory of Advanced Display and System Applications of Ministry of Education, Shanghai University, Shanghai 200072, China

^b CAS Key Laboratory of Crust-Mantle Materials and Environments, School of Earth and Space Sciences, University of Science and Technology of China, Hefei 230026, China

^c Henan Key Laboratory of Photovoltaic Materials, Henan University, Kaifeng 475004, China

^d Faculty of Engineering, University of Nottingham, Nottingham NG72RD, UK

^e Center for Optoelectronic Engineering Research, Department of Physics, School of Physics and Astronomy, Yunnan University, Kunming 650091, China

ARTICLE INFO

Article history:

Received 31 August 2021

Received in revised form 17 October 2021

Accepted 7 December 2021

Available online xxxxx

Keywords:

Light-emitting field-effect transistors

Quantum dots

Electroluminescence

External quantum efficiency

ABSTRACT

Emerging quantum dots (QDs) based light-emitting field-effect transistors (QLEFETs) could generate light emission with high color purity and provide facile route to tune optoelectronic properties at a low fabrication cost. Considerable efforts have been devoted to designing device structure and to understanding the underlying physics, yet the overall performance of QLEFETs remains low due to the charge/exciton loss at the interface and the large band offset of a QD layer with respect to the adjacent carrier transport layers. Here, we report highly efficient QLEFETs with an external quantum efficiency (EQE) of over 20% by employing a dielectric-QDs-dielectric (DQD) sandwich structure. Such DQD structure is used to control the carrier behavior by modulating energy band alignment, thus shifting the exciton recombination zone into the emissive layer. Also, enhanced radiative recombination is achieved by preventing the exciton loss due to presence of surface traps and the luminescence quenching induced by interfacial charge transfer. The DQD sandwiched design presents a new concept to improve the electroluminescence performance of QLEFETs, which can be transferred to other material systems and hence can facilitate exploitation of QDs in a new type of optoelectronic devices.

© 2021 Science China Press. Published by Elsevier B.V. and Science China Press. All rights reserved.

1. Introduction

Light-emitting field-effect transistors (LEFETs) show tunable optoelectronic properties dependent on the electrostatic gating induced by a combination of light emission and switching capacity, and have a great potential for applications in display, integrated optical communication, and electrically driven lasers, etc. [1–11]. In the past few years, organic LEFETs have been reported with different geometries including single-layer, bilayer and multilayer heterojunction structures, aiming to enhance the device performance and understand the carrier transport mechanisms [3,7,12–14]. The LEFETs with multilayer heterojunction demonstrate suppressed electrode-induced photon loss, and metal-exciton and charge-exciton interactions, which are unavoidable in the single-layer or bilayer systems [15–25]. Hence multilayer heterojunctions

are considered as promising structures for improved electroluminescence (EL) performance of LEFETs.

Quantum dots (QDs) have been successfully integrated into the LEFETs (QLEFETs) and offer advantages of high color purity and tunability, as well as solution-processable fabrication [8,11,26–30]. However, the progress made with QLEFETs is still limited, especially in the blue and green QLEFETs. To date, the QLEFETs with the emission wavelengths below 550 nm show the external quantum efficiencies (EQEs) of only less than 12% [29]. In these devices, the interfacial contact is known to have a critical effect on optoelectronic performance, especially for the in-plane top-contact source-drain electrode structures [12,31]. When both source and drain electrodes are deposited on the top of the carrier transport layer (CTL), the in-plane field is generated to facilitate the carrier transport from the top layer preferentially. The efficient carrier transport from the CTL to the QD emissive layer (EML) is prevented by large band offset or poor interfacial contact. Therefore, a high source-drain voltage is imperative to realize efficient carrier

* Corresponding authors.

E-mail address: yangxy@shu.edu.cn (X. Yang).

<https://doi.org/10.1016/j.scib.2021.12.013>

2095-9273/© 2021 Science China Press. Published by Elsevier B.V. and Science China Press. All rights reserved.

injection [32–40], however it leads to the reduced device lifetime and possible increase in energy consumption.

Here, we report a solution processable high-performance green QLEFETs based on dielectric-EML-dielectric sandwich structure, namely, methylammonium bromine (MABr)-QDs-polyethylenimine ethoxylated (PEIE). In these dielectric-QDs-dielectric (DQD) structures, the PEIE thin layer on the QDs is used to create a favourable valence band offset and to improve the interfacial contact between the QDs and the hole transport layer (HTL), which makes the exciton recombination zone shift into the QDs emissive layer. The MABr thin layer below the QD layer is introduced to enhance the electron transport by passivating the surface defects on ZnO nanoparticles electron transport layer (ETL) and to suppress the luminescence quenching of the QDs layer induced by interfacial charge transfer. We perform a comprehensive evaluation of the performance of these QLEFET devices and support our findings by the density functional theory (DFT) studies, and demonstrate that the device concept proposed here enables to produce structures with favourable energy level alignment and an improved interfacial contact. The green QLEFETs with the DQD structure developed here demonstrate a record-high current efficiency (CE) of 93.6 cd A⁻¹ corresponding to an EQE of 21%.

2. Experimental

2.1. Materials

The CdSe/ZnS QDs dispersed in octane were purchased from Mesolight Inc. The average nanocrystal size is ~ 10 nm, the shell thickness is ~ 3 nm, the surface ligands are mainly oleic acid, and the PLQY is > 90%. The aqueous solution (37 wt%) of PEIE, MABr (98%), and dimethyl sulfoxide (DMSO, 99.9%) were purchased from Sigma-Aldrich. Al4083 PEDOT:PSS (Clevis P VP Al4083) was modified by mixing it 1:1 v/v with isopropyl alcohol.

2.2. Synthesis of ZnO nanoparticles solution

A low-temperature solution-precipitation method was used to synthesize ZnO nanoparticles [41]. Briefly, 3 mmol anhydrous zinc acetate was mixed with 30 mL DMSO. 5.5 mmol tetramethylammonium hydroxide dissolved in 10 mL ethanol was added drop-wise into the zinc acetate solution, stirred for 1 h at room temperature. The formed ZnO nanoparticles were collected by centrifugation, washed with ethyl acetate twice and re-dispersed in ethanol. The solutions were filtered before use.

2.3. Device fabrication

The indium tin oxide (ITO)-coated glass substrates were cleaned in an ultrasonic bath consecutively using detergent, deionized water, acetone and isopropanol, for 30 min each. Then, a layer of insulating Al₂O₃ (150 nm) was deposited at 200 °C by atomic layer deposition (ALD) using alternating exposure to Al(CH₃)₃ and H₂O vapor at a deposition rate of 0.66 Å per cycle. Subsequently, the coated substrates were transferred into an N₂-filled glove box for spin-coating of ZnO nanoparticles, MABr, QDs, PEIE and PEDOT:PSS. The ZnO nanoparticles solution (30 mg mL⁻¹) was spin coated at 2000 r min⁻¹ for 40 s and annealed at 150 °C for 30 min. The MABr dissolved in DMSO (0.3, 0.5 and 1.0 mg mL⁻¹) was spin coated onto ZnO layer and annealed at 100 °C for 10 min. The QD layer was prepared by spin coating the QD solution (18 mg mL⁻¹) onto MABr at 2000 r min⁻¹ for 40 s and annealing at 90 °C for 20 min. The PEIE (diluted with 2-ethoxyethanol to 0.8% w/v) was spin coated onto QDs and annealed at 120 °C for 20 min. PEDOT:PSS solution was spin-coated onto PEIE at

4000 r min⁻¹ and annealed at 130 °C for 20 min. Finally, the Aluminum (Al) layer (120 nm) was deposited through a shadow mask by thermal evaporation under a based vacuum (≈ 10⁻⁴ Pa) to form the source and drain electrodes with the channel width of 1000 μm and channel length of 50 μm.

2.4. Characterization

The *I*-*V* characteristics of QLEFETs were acquired by a semiconductor parameter analyzer (Keithley 4200) with a probe station (LakeShore, TTP4). A photomultiplier tube, PMT, R928 (Hamamatsu) was placed over the devices and used for simultaneous light-intensity measurements. The photomultiplier is calibrated by an optical integrating sphere [42]. The EL spectra were acquired using Ocean Optics spectrometer. The luminance was obtained by combining the photocurrent collected from the drain electrode with that of QD light-emitting diodes (QLEDs) using the following equation: $\frac{L_{\text{QLED}}}{L_{\text{QLEFET}}} \frac{S_{\text{QLED}}}{S_{\text{QLEFET}}} = \frac{I_{\text{QLED}}^{\text{P}}}{I_{\text{QLEFET}}^{\text{P}}}$ where *L* is the luminance, *S* is the emission area, and *I*^P is the photocurrent of the devices, respectively. The current density was calculated as the channel current divided by its area. The EQE was calculated from the luminance, the drain-source current (*I*_{DS}), and the EL emission spectrum. The carrier mobilities were calculated using the formula for the linear regime: $\mu = L/W \frac{1}{C_g V_{\text{DS}}} \frac{\delta I_{\text{DS}}}{\delta V_{\text{GS}}}$ where μ is the field-effect mobility, *C_g* is the gate dielectric capacitance density and *W* and *L* are the channel width (1000 μm) and length (50 μm), respectively. The cross-sectional transmission electron microscopy (TEM) was performed on a dual-beam focused ion beam with scanning electron microscopy (SEM) and Omniprobe AutoProbe 200.2 robotic hand. The X-ray photoelectron spectroscopy (XPS) data were collected using an ESCALAB 250Xi (Thermo) system. The work functions of the samples were determined by ultraviolet photoelectron spectroscopy (UPS, ESCALAB 250Xi). Absorption spectra were obtained using a PerkinElmer Lambda 950 UV-vis-NIR spectrometer. The photoluminescence (PL) spectra and time-resolved PL (TRPL) were measured using an Edinburgh FLS920 spectrometer. The surface morphology of the films was measured using atomic force microscope (AFM, Seiko SPA 400) and field emission scanning electron microscopy (JSM-6701F). All measurements were performed at room temperature under ambient conditions.

2.5. DFT simulations

DFT calculations were performed using the Vienna *Ab initio* Simulations Package (VASP) [43,44] and projected augmented wave (PAW) method [45–47]. The exchange–correlation interaction was treated with generalized gradient approximation (GGA) in the Perdew, Burke and Ernzerhof (PBE) [48] parameterization. For strongly localized *d* electrons, GGA has systematic and noncancelling errors [49]. Therefore, we adopted GGA + *U* (*U* = 8 and *J* = 1) [50,51] to correct for the self-interaction and over delocalized *d* states. The cut-off energy of the plane-wave basis was set to 450 eV, and integrations over the first Brillouin zone were calculated using a Gamma-centred *k*-point set of 6 × 6 × 4. With these settings, the total energy converged within 1 meV/atom. The wurtzite ZnO (space group *P6₃mc*, No. 186) structure was fully relaxed using GGA + *U*; the energy was converged within 10⁻⁶ eV cell⁻¹ and the force was converged to less than 10⁻³ eV Å⁻¹. A vacuum spacing no less than 15 Å was used in all slab calculations with the same cut-off energy and similar *k*-point density to that used for bulk calculations. The (100) surface was modelled by a six-layer slab consisting of 144 atoms. The bottom three layers were fixed during relaxation. A Schottky defect was created on the top layer. The adsorption energies of MABr on the perfect surface

and defective surface were calculated to be 0.9 and 2.1 eV, respectively.

3. Results and discussion

3.1. Device structure and performance

Multilayer heterojunction structures were deposited onto ITO-coated glass by layer-by-layer solution processing. Fig. 1a schematically displays our top-contact QLEFETs with stacked trilayer of ETL, EML, and HTL. In this device, the CdSe/ZnS QDs layer, serving as EML, is sandwiched between dielectric layers of PEIE and MABr to form the DQD structure. The PEDOT:PSS and ZnO are used as the HTL and the ETL, respectively. Al source and the drain electrodes are deposited onto the PEDOT:PSS layer. The channel width and length are 1000 and 50 μm , respectively (see a photograph and an optical microscopy image in Fig. S1 online). As revealed by a cross-sectional SEM image, the functional layers are well defined and compact even after multiple solution processing steps (Fig. 1b). The device architecture and composition were further assessed by energy dispersive spectroscopy (EDS) (Fig. 1c) and high-resolution TEM (Fig. 1d), demonstrating that the thicknesses of PEIE, QDs, and MABr layers in the DQD sandwich structure are ~ 5 , 25 and ~ 3 nm, respectively.

The EL spectrum of the resulting QLEFETs revealed a narrow peak centered at $\lambda_{\text{EL}} \sim 534$ nm with a full-width-at-half-maximum (FWHM) = 28 nm (Fig. 2a), which indicates a color-saturated green emission. The EL spectrum is slightly red-shifted

and broadened compared with the PL spectrum of the QD solution ($\lambda_{\text{PL}} \sim 530$ nm with a FWHM = 21 nm), resulting from the interdot interactions and electric field-induced quantum confinement Stark effect [52]. The green emission observed from the operating device with DQD structure is significantly brighter than that from the device without DQD structure (see the inset in Fig. 2a), suggesting an improved carrier injection and enhanced radiative recombination.

The electrical properties of QLEFETs with a QDs-only layer (control device), QDs/PEIE and MABr/QDs/PEIE were investigated in ambient conditions. The gate voltage (V_{GS}) was swept from -60 to 60 V with applied drain voltage ($V_{\text{DS}} = 20$ V). A characteristic unipolar p -type behavior is observed in the control device (Fig. 2b, purple circles), suggesting a hole-dominated charge transport in this trilayer structure. The field effect transistor (FET) with a PEDOT:PSS-only layer (Fig. S2a online) demonstrates a very similar hole transport characteristics to that of the control device, indicating that the injected holes are predominantly transported across the top p -type CTL (PEDOT:PSS). To further confirm the mechanism of charge transport, the Mott-Schottky curves were measured under dark conditions (Fig. 2c). A negative slope observed in the control device suggests a p -type conductivity characteristic, confirming the results of electrical transfer characteristics. However, there is a significant difference in the QLEFETs with a thin layer of PEIE deposited on QDs, which show a characteristic ambipolar behavior. This suggests the charge transport from HTL to the QD EML, which is also observed in the QDs-only FET (Fig. S2b online). The electrical transfer characteristics under forward/reverse sweep

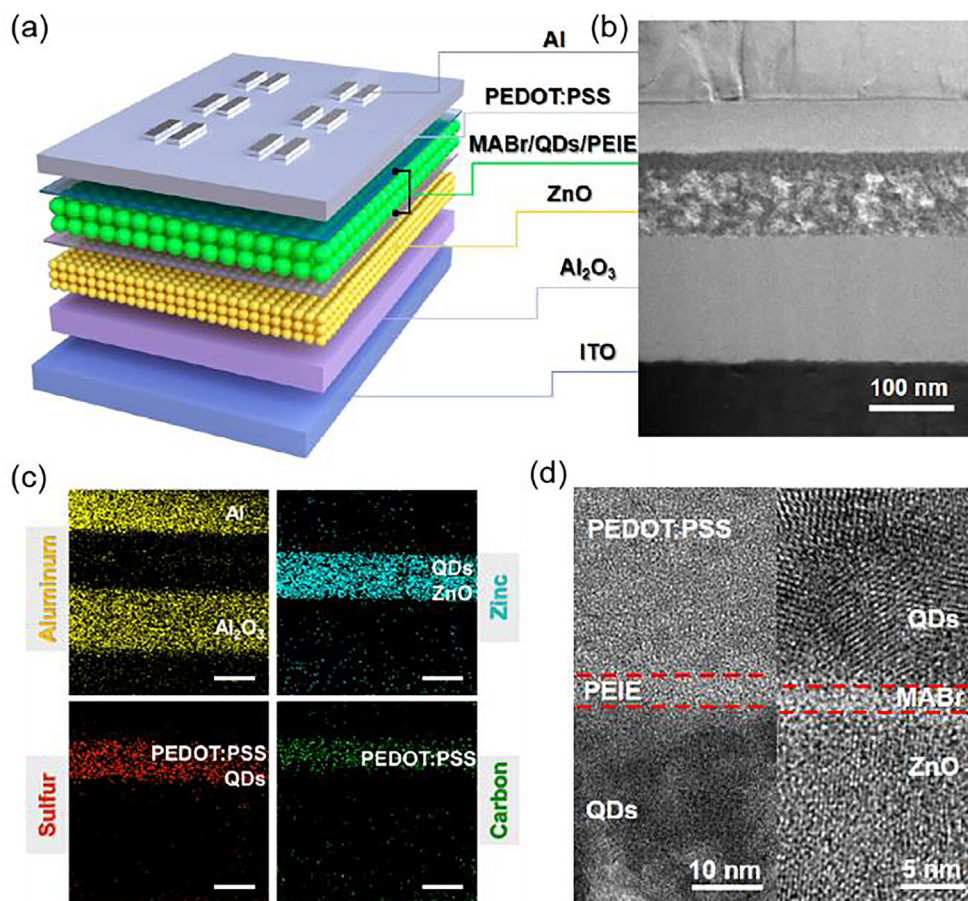


Fig. 1. (Color online) Device structure of QLEFETs with an emission layer of CdSe/ZnS QDs. (a) Schematic diagram of the device structure, (b) cross-sectional SEM image and (c) EDS compositional mapping images of a QLEFET with a DQD sandwiched structure. The scale bars are 100 nm. The thicknesses of Al_2O_3 , ZnO, and PEDOT:PSS layer are ~ 150 , 80 and 60 nm, respectively. (d) Representative high-resolution TEM images of cross-sections of (left) QDs/PEIE/PEDOT:PSS and (right) ZnO/MABr/QDs heterostructures.

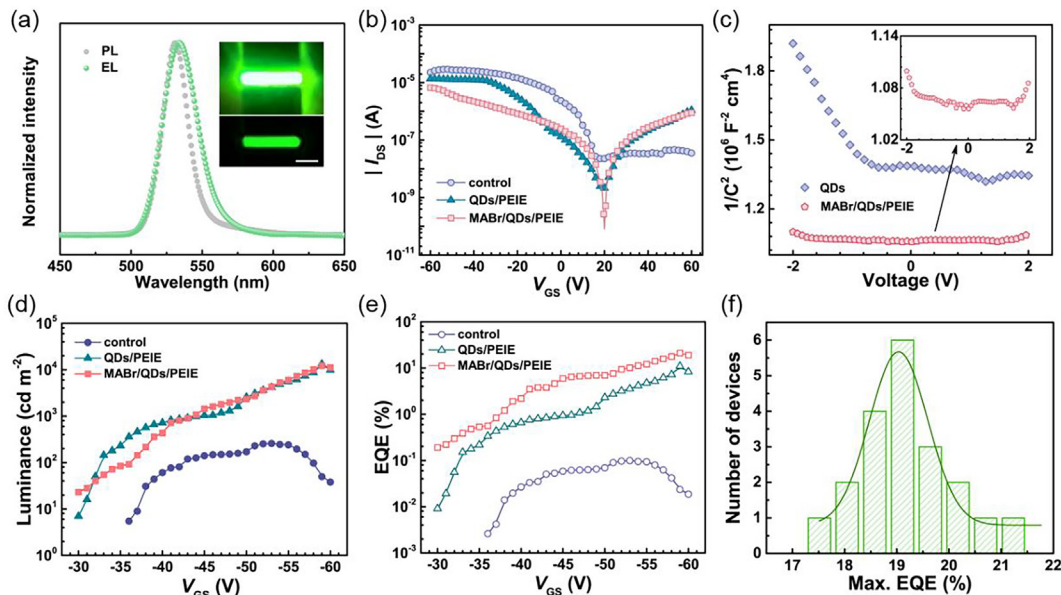


Fig. 2. (Color online) Performance characterization of QLEFETs. (a) Normalized PL and EL spectra of QLEFET with a DQD sandwich structure. Inset: the photograph of the operating devices with (top) and without (bottom) the DQD structure. The emitting area is $1 \text{ mm} \times 0.05 \text{ mm}$ at $V_{DS} = -50 \text{ V}$. The scale bar is $400 \mu\text{m}$. (b) Electrical transfer characteristics of the QLEFETs. (c) Mott-Schottky plots of the control and QLEFETs with DQD structure. (d) Luminance (L)- V_{GS} and (e) EQE- V_{GS} of the QLEFETs. (f) Histogram of the maximum EQEs measured on 20 devices.

and at different drain voltages (Fig. S3 online) confirmed the ambipolar behaviour of the PEIE based QLEFETs, consistent with the transfer characteristics observed in these structures (Fig. S4 online).

The device performance was assessed by the measurements of luminance, CE and EQE. For the control device at $V_{DS} = 20 \text{ V}$, the following values were measured: highest values of luminance of 260 cd m^{-2} , CE = 0.44 cd A^{-1} and EQE = 0.1% at the gate voltage of -53 V (Fig. 2d), e and Fig. S5 online). Following deposition of the PEIE layer onto the QDs layer, the device performance was significantly improved, reaching the maximum luminance of $13,320 \text{ cd m}^{-2}$, CE = 49.0 cd A^{-1} and EQE = 11%. This enhancement of device performance was attributed to the optimized hole transport in the emissive layer. The gate leakage current of the device modified with PEIE (Fig. S6 online) is smaller than I_{DS} under the same applied V_{GS} , hence it has a negligible impact on the device performance. Therefore, the observed significant improvement of the EL emission is mainly attributed to the enhanced radiative recombination resulting from the efficient injection of holes into the EML. The efficient hole injection could be ascribed to two main reasons: the improved QDs/PEDOT:PSS interfacial contact and the reduced energy barrier between the QDs and PEDOT:PSS in the presence of the PEIE interlayer. The detailed analysis of the interface and the energy band realignment before and after inserting PEIE is discussed below.

In the presence of a thin layer of MABr, the electron transport is further improved due to the enhancement of radiation recombination rate in the QDs layer. The devices with PEIE and MABr layers exhibit both the negative and the positive slopes in the Mott-Schottky plots, characteristic of an ambipolar behaviour with the hole and electron field-effect mobilities of $8.38 \times 10^{-4} \text{ cm}^2 \text{ V}^{-1} \text{ s}^{-1}$ at $V_{DS} = 20 \text{ V}$, $V_{GS} = -25 \text{ V}$ and $7.82 \times 10^{-4} \text{ cm}^2 \text{ V}^{-1} \text{ s}^{-1}$ at $V_{DS} = 20 \text{ V}$, $V_{GS} = 25 \text{ V}$, respectively. With the incorporation of MABr layer deposited on ZnO, the best EL performance is observed for the QLEFETs with the DQD structure (see Figs. S7, S8 online), with the maximum luminance of $12,240 \text{ cd m}^{-2}$, EQE = 21% and CE = 93.6 cd A^{-1} . The devices also show good reproducibility with an average EQE of 19% (Fig. 2f).

3.2. DQD structure characteristics

To gain further insights into the contribution of the DQD structure in improving the QLEFETs performance, the role of PEIE and MABr layers was studied. AFM, SEM, and UPS measurements were carried out to investigate the surface morphology and the energy levels of the QDs and QDs/PEIE films. The interface morphology and alignment of energy levels are the critical parameters defining the carrier transport. It is also noteworthy that surface defects on the nanoparticles can act as charge traps leading to non-radiative recombination. The QD layer in these devices is relatively thin ($\sim 25 \text{ nm}$), and hence pinholes can be formed easily during solution-based processing and the deposition onto the ZnO film with a relatively high surface roughness [53]. The pinholes in the QDs layer may lead to the direct contact between the HTL and the ETL, having a detrimental effect on the device performance. The AFM images (Fig. 3a-c) revealed the maximum height amplitude in the ZnO underlayer and the QDs layer of ~ 10 and $\sim 13 \text{ nm}$, respectively. When the PEIE thin layer is introduced between QDs and PEDOT:PSS, a decrease of the height amplitude of QD film to 3 nm . This corresponds to a decrease of the root mean square (r.m.s.) value of the surface roughness from 1.25 to 0.42 nm , confirming the formation of a smooth film surface without pinholes. Note that the thickness of PEIE is reduced when the PEDOT:PSS is deposited on top of it due to the partial dissolution of PEIE surface caused by the solvent used. The improved interfacial quality is consistent with the SEM results (Fig. S9 online). These results confirm that the coating with PEIE could improve the interface morphology, hence preventing the carrier loss at the contact of the CTLs. In addition, the PEIE helps to modify the electronic structure of the QDs (Fig. 3f) resulting from the formation of interface dipoles by taking advantage of its aliphatic amine groups with large dipole moment [54,55]. The UPS data for the QD films (Fig. 3d, e) and Fig. S10 online) revealed a decreased work function (from 4.1 to 3.9 eV) and a shift of the valence band maximum (VBM) from 6.0 to 5.8 eV , which reduces the energy barrier at the QDs/PEDOT:PSS interface and thus enhances hole injection capability. This optimized band energy alignment is of great

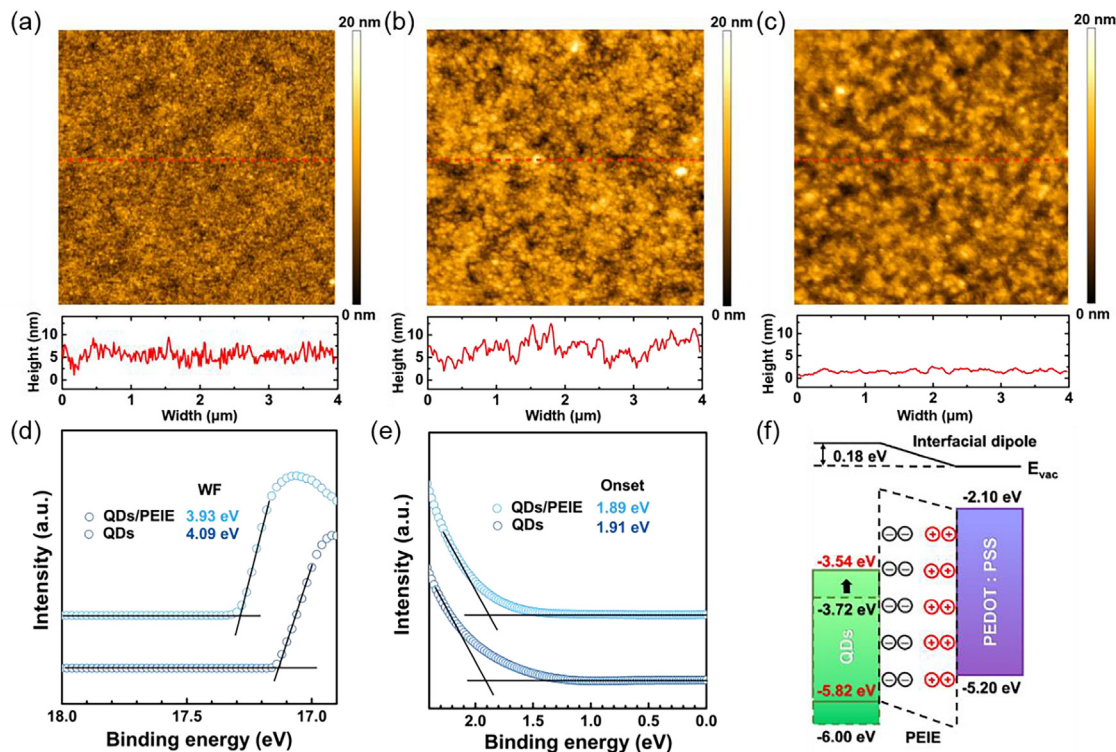


Fig. 3. (Color online) Assessment of morphology and energy level alignment of the QD films. AFM images and a representative z-profile of (a) ZnO, (b) QDs and (c) QDs/PEIE films. UPS spectra in (d) secondary electron region and (e) frontier electronic structure region of the QDs and the QDs/PEIE films. (f) Schematic diagram of energy level alignment in the PEIE modified QD films, where E_{vac} is the vacuum energy.

importance for hole injection from the HTL to EML, which makes the recombination region of excitons shift into the QDs EML and therefore, leads to the great improvement of the EL performance (see schematic diagram of carrier transport in Fig. S11 online).

The optical properties of MABr/QDs films were investigated to understand the role of MABr in QLEFETs. As shown in Fig. 4a, the PL emission intensity of the QD films is significantly decreased when being in contact with the conductive ZnO layer. The observed

decrease of PL intensity is attributed to charge transfer at the interface of ZnO/QDs; while the PL quenching is effectively suppressed when a thin layer of MABr is inserted. It is known that ZnO nanoparticles with high surface-to-volume ratios introduces numerous surface defects, which can act as electron trapping and charge recombination sites [56,57]. The ZnO/MABr/QDs film displays a longer PL lifetime than that of ZnO/QDs film (Fig. 4b and Table S1 online), indicating the reduced interfacial non-radiative

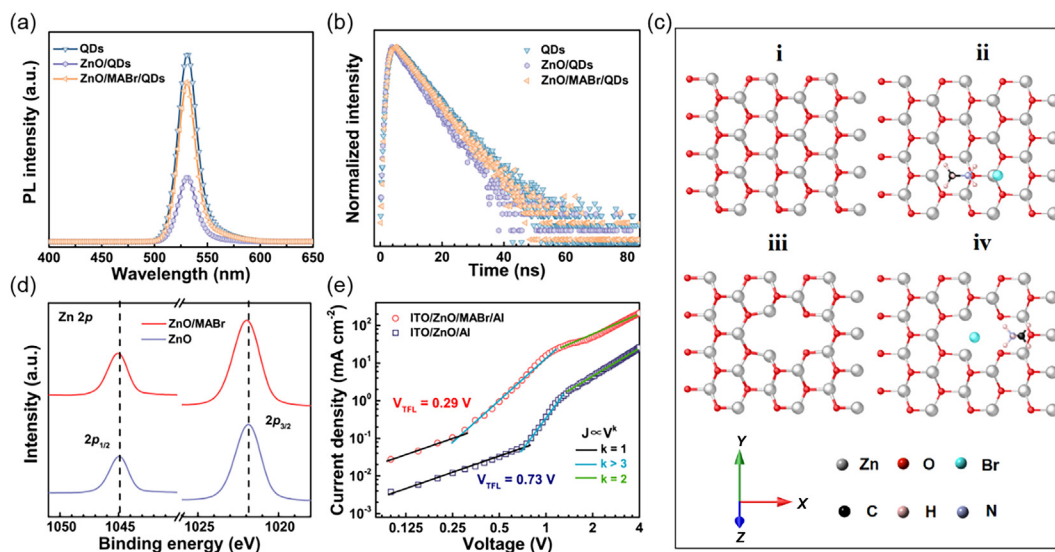


Fig. 4. (Color online) Optical characteristics of the QDs/ZnO film and trap densities characteristics of the ZnO film. (a) PL spectra and (b) TRPL decay curves of the QDs, ZnO/QDs and ZnO/MABr/QDs films coated on the glass substrate. Spectra were acquired under excitation with 365 nm. (c) Ball-and-stick model of the top layer of (i) wurtzite ZnO (100) surface, (ii) ZnO (100) surface with adsorbed MABr, (iii) ZnO (100) surface with one Schottky defect and (iv) ZnO (100) surface with MABr adsorbed at the Schottky defect. (d) XPS spectra of the ZnO and ZnO/MABr films. (e) Current density (J)– V curves for devices with structures of ITO/ZnO/MABr/Al and ITO/ZnO/Al.

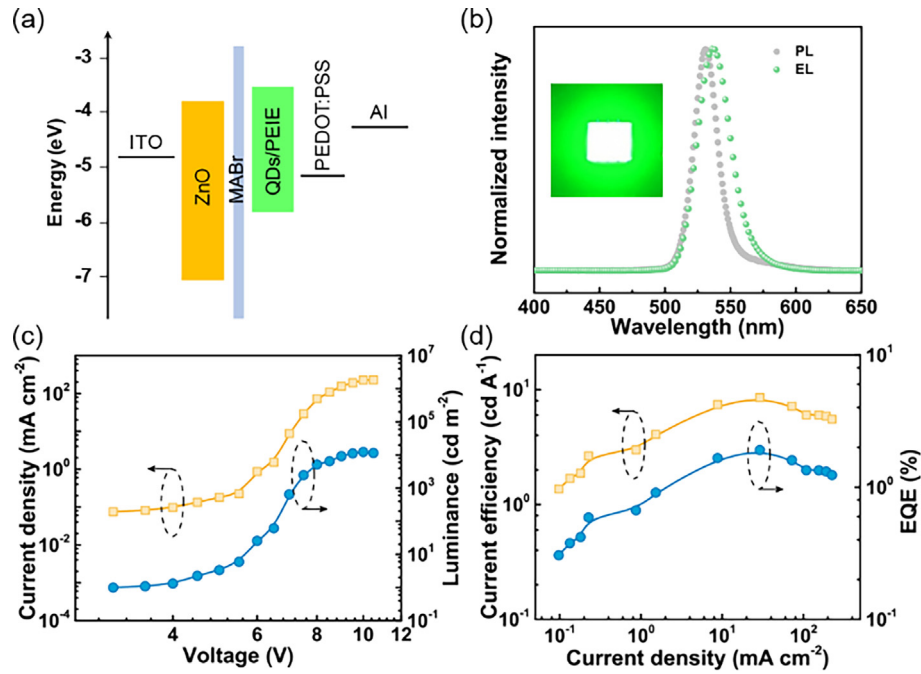


Fig. 5. (Color online) Device structure and performance characterization of QLEDs. (a) Energy level diagram of the QLEDs. (b) Normalized EL and PL spectra, (c) J - V - L characteristics and (d) CE- J -EQE characteristics of QLEDs. Inset in (b): the photograph of the operating device with an emitting area of 2 mm \times 2 mm at applied voltage of 7.5 V.

recombination. DFT calculations reveal that Schottky defects are easily formed on the surface of ZnO. The adsorption energies for MABr on the perfect surface and defect-rich surface are calculated to be 0.9 and 2.1 eV, respectively (see Experimental). As shown in Fig. 4c (iii and iv), the positions of atoms and bond angles on the defect-rich surface with adsorbed MABr are comparable to those of the perfect surface without MABr. This chemical bonding between the MABr and a Schottky defect significantly reduces the charge-carrier trapping induced by oxygen vacancies [57]. The coordination between Zn^{2+} and Br^- has also been experimentally confirmed by XPS results (Fig. 4d), where the photoemission of $\text{Zn } 2p_{1/2}$ and $\text{Zn } 2p_{3/2}$ in the ZnO/MABr film are both shifted to higher binding energies by around 0.3 eV in comparison with that of ZnO film, demonstrating that Br^- is bound to Zn^{2+} .

To demonstrate the trap states intuitively, the subthreshold swing (SS) without and with MABr modification were obtained to be 5.2 and 1.1 V dec^{-1} , respectively, through the output characteristics at the V_{DS} voltage of 20 V (Note S1 in the Supplementary materials). We calculated the interface trap density (D_{IT}) with the equation, $D_{\text{IT}} = \frac{C_i}{q} \left(\frac{q \cdot \text{SS}}{K_B T \cdot \ln 10} - 1 \right)$ where C_i , K_B , T , and q are the dielectric capacitance, Boltzmann constant, temperature, electron charge, respectively. The D_{IT} for QLEFET without and with MABr layer is calculated to be 3.2×10^{13} and $6.3 \times 10^{12} \text{ cm}^{-2} \text{ eV}^{-1}$, respectively.

We further performed the trap-filled space-charge-limited current studies to quantify the trap density in ZnO layer without and with the MABr interlayer (Fig. 4e). The current density increases linearly in the ohmic regime. The nonlinear regimes are correlated with a trap-filled limited and space charge limited current according to k ($J \propto V^k$) [58–60]. The trap-state density (n_{trap}) can be determined by the equation: $n_{\text{trap}} = \frac{2\epsilon\epsilon_0 V_{\text{TFL}}}{eL^2}$, where ϵ is the relative dielectric constant of ZnO, ϵ_0 is the permittivity of free-space, V_{TFL} is trap-filled limiting voltage, e is the elementary charge, and L is the thickness of the ZnO film. It is found that the MABr interlayer reduces the trap density from $2.1 \times 10^{17} \text{ cm}^{-3}$ for ZnO film to

$8.5 \times 10^{16} \text{ cm}^{-3}$ for ZnO/MABr film, which thus results in a higher electron current in the electron-only device with ZnO/MABr structure.

3.3. QLEDs with a DQD structure

To understand the gating effect on the luminescence emission, the comparison of the device performance parameters of the QLEFETs and QLEDs was conducted. The QLEDs with the same structure and composition of the active layers were fabricated (Fig. 5a), in which the layer sequence, thickness and growth parameters are the same as those in the QLEFETs. The energy levels of the ZnO films are calculated from the UPS and optical studies (Fig. S12 online). Since the work functions of Al and ITO are similar, the transport behaviors of carriers in the QLEDs can be compared to those in the QLEFETs. The EL spectrum of QLEDs revealed a peak at $\lambda_{\text{EL}} \sim 534 \text{ nm}$ with FWHM = 30 nm (Fig. 5b), similar to that of the QLEFETs (Fig. 2). The QLEDs with DQD structure demonstrate a characteristic I - V LED behavior, showing a maximum brightness of $12,400 \text{ cd m}^{-2}$, CE = 8.5 cd A^{-1} and EQE = 1.9% (Fig. 5c, d). Note that the relatively low performance for the QLED is mainly due to a poor charge balance in this device in the absence of a HTL (i.e., poly[bis(4-phenyl)(4-butylphenyl)amine] (poly-TPD), poly(9-vinyl carbazole) (PVK) and poly(9,9-dioctylfluorene-alt-N-(4-secbutylphenyl)-diphenylamine) (TFB), etc.). We envisage that the superior performance in QLEFETs, including luminance and EQE, results from the effective electron injection from ZnO into the QD layer induced by the gating effect. As the V_{GS} increases, the electrons transport from ZnO into QDs will be promoted, which favors the radiative recombination of excitons and the subsequent light emission. The luminance and EQE under different negative gate voltages were also investigated and support this explanation (Fig. S13 online). Both the luminance and EQE consistently increase with the increase of the negative gate voltage, which demonstrates that the gating effect greatly improves the electron transport from ZnO

to QDs. As a result, an EL generating device with one-order of magnitude higher efficiency is realized in a DQD structure-based QLE-FETs, owing to the improved carrier transport balance.

4. Conclusion

In summary, we have demonstrated a high-performance QLE-FET with an EQE up to 21% by employing a concept of DQD structure, PEIE-QDs-MABr. The PEIE with a high dipole moment modifies the interface of the QDs and PEDOT:PSS effectively, resulting in a smooth interfacial morphology and a better energy alignment between the QDs and PEDOT:PSS. These enable the exciton recombination zone to move to the interior of QDs emissive layer, consequently leading to a significant improvement of the device performance. In these devices, the thin layer of MABr acts to reduce the electron trapping on the ZnO surface, which increases the electron density in QD layer and suppresses the PL quenching of emissive layer. Thus, we are able to achieve the green QLEFETs with highest efficiency reported to date. Our work paves the way for the development of high-performance QLEFETs and their future applications.

Conflict of interest

The authors declare that they have no conflict of interest.

Acknowledgments

We acknowledge financial support from the National Natural Science Foundation of China (62174104, 61735004, and 12174086), the National Key Research and Development Program of China (2016YFB0401702), and the Shanghai Science and Technology Committee (19010500600).

Appendix A. Supplementary materials

Supplementary materials to this article can be found online at <https://doi.org/10.1016/j.scib.2021.12.013>.

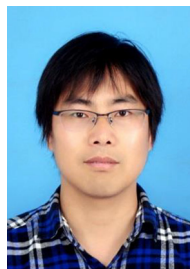
References

- Muccini M. A bright future for organic field-effect transistors. *Nat Mater* 2006;5:605–13.
- Namdas EB, Tong M, Ledochowitsch P, et al. Low thresholds in polymer lasers on conductive substrates by distributed feedback nanoimprinting: progress toward electrically pumped plastic lasers. *Adv Mater* 2009;21:799–802.
- Ullah M, Tandy K, Yambem SD, et al. Simultaneous enhancement of brightness, efficiency, and switching in RGB organic light emitting transistors. *Adv Mater* 2013;25:6213–8.
- McCarthy MA, Liu B, Donoghue EP, et al. Low-voltage, low-power, organic light-emitting transistors for active matrix displays. *Science* 2011;332:570–3.
- Yu H, Kim D, Lee J, et al. High-gain infrared-to-visible upconversion light-emitting phototransistors. *Nat Photonics* 2016;10:129–34.
- Chin XY, Cortecchia D, Yin J, et al. Lead iodide perovskite light-emitting field-effect transistor. *Nat Commun* 2015;6:7383.
- Muhieddine K, Ullah M, Pal BN, et al. All solution-processed, hybrid light emitting field-effect transistors. *Adv Mater* 2014;26:6410–5.
- He P, Lan L, Deng C, et al. Highly efficient and stable hybrid quantum-dot light-emitting field-effect transistors. *Mater Horiz* 2020;7:2439–49.
- Ullah M, Wawrzinek R, Maasoumi F, et al. Semitransparent and low-voltage operating organic light-emitting field-effect transistors processed at low temperatures. *Adv Opt Mater* 2016;4:1022–6.
- Namdas EB, Hsu BBY, Yuen JD, et al. Optoelectronic gate dielectrics for high brightness and high-efficiency light-emitting transistors. *Adv Mater* 2011;23:2353.
- Kahmann S, Shulga A, Loi MA. Quantum dot light-emitting transistors—powerful research tools and their future applications. *Adv Funct Mater* 2020;30:1904174.
- Chaudhry MU, Muhieddine K, Wawrzinek R, et al. Organic light-emitting transistors: advances and perspectives. *Adv Funct Mater* 2020;30:1905282.
- Namdas EB, Ledochowitsch P, Yuen JD, et al. High performance light emitting transistors. *Appl Phys Lett* 2008;92:183304.
- Capelli R, Toffanin S, Generali G, et al. Organic light-emitting transistors with an efficiency that outperforms the equivalent light-emitting diodes. *Nat Mater* 2010;9:496–503.
- Liu C-F, Liu X, Lai W-Y, et al. Organic light-emitting field-effect transistors: device geometries and fabrication techniques. *Adv Mater* 2018;30:1802466.
- Zhang C, Chen P, Hu W. Organic light-emitting transistors: materials, device configurations, and operations. *Small* 2016;12:1252–94.
- Swensen JS, Soci C, Heeger AJ. Light emission from an ambipolar semiconducting polymer field-effect transistor. *Appl Phys Lett* 2005;87:253511.
- Zaumseil J, Friend RH, Sirringhaus H. Spatial control of the recombination zone in an ambipolar light-emitting organic transistor. *Nat Mater* 2006;5:69–74.
- Bisri SZ, Takenobu T, Yomogida Y, et al. High mobility and luminescent efficiency in organic single-crystal light-emitting transistors. *Adv Funct Mater* 2009;19:1728–35.
- Zaumseil J, Donley CL, Kim J-S, et al. Efficient top-gate, ambipolar, light-emitting field-effect transistors based on a green-light-emitting polyfluorene. *Adv Mater* 2006;18:2708–12.
- Schildleja M, Melzer C, von Seggern H. Electroluminescence from a pentacene based ambipolar organic field-effect transistor. *Appl Phys Lett* 2009;94:123307.
- Wang Y, Kumashiro R, Nouchi R, et al. Influence of interface modifications on carrier mobilities in rubrene single crystal ambipolar field-effect transistors. *J Appl Phys* 2009;105:124912.
- Ke T-H, Gehlhaar R, Chen C-H, et al. High efficiency blue light emitting unipolar transistor incorporating multifunctional electrodes. *Appl Phys Lett* 2009;94:1533071.
- Suganuma N, Shimoji N, Oku Y, et al. Novel organic light-emitting transistors with PN-heteroboundary carrier recombination sites fabricated by lift-off patterning of organic semiconductor thin-films. *J Mater Res* 2007;22:2982–6.
- Lu C, Ji Z, Xu G, et al. Progress in flexible organic thin-film transistors and integrated circuits. *Sci Bull* 2016;61:1081–96.
- Yang D, Li X, Zhou W, et al. CsPbBr₃ Quantum qots 2.0: benzenesulfonic acid equivalent ligand awakens complete purification. *Adv Mater* 2019;31:1900767.
- Song J, Li J, Li X, et al. Quantum dot light-emitting diodes based on inorganic perovskite cesium lead halides (CsPbX₃). *Adv Mater* 2015;27:7162–7.
- Chen J, Wang J, Xu X, et al. Efficient and bright white light-emitting diodes based on single-layer heterophase halide perovskites. *Nat Photonics* 2021;15:238–44.
- Liu X, Kuang W, Ni H, et al. High efficiency light-emitting transistor with vertical metal-oxide heterostructure. *Small* 2018;14:1800265.
- Fang T, Wang T, Li X, et al. Perovskite QLED with an external quantum efficiency of over 21% by modulating electronic transport. *Sci Bull* 2021;66:36–43.
- Chen Q, Yan Y, Wu X, et al. High-performance quantum-dot light-emitting transistors based on vertical organic thin-film transistors. *ACS Appl Mater Interfaces* 2019;11:35888–95.
- Natali M, Quiroga SD, Passoni L, et al. Simultaneous tenfold brightness enhancement and emitted-light spectral tunability in transparent ambipolar organic light-emitting transistor by integration of high-k photonic crystal. *Adv Funct Mater* 2017;27:1605164.
- Ullah M, Wawrzinek R, Nagiri RCR, et al. UV-deep blue-visible light-emitting organic field effect transistors with high charge carrier mobilities. *Adv Opt Mater* 2017;5:1600973.
- Maruyama K, Sawabe K, Sakanoue T, et al. Ambipolar light-emitting organic single-crystal transistors with a grating resonator. *Sci Rep* 2015;5:10221.
- Hsu BBY, Seifert J, Takacs CJ, et al. Ordered polymer nanofibers enhance output brightness in bilayer light-emitting field-effect transistors. *ACS Nano* 2013;7:2344–51.
- Schornbaum J, Zakharko Y, Held M, et al. Light-emitting quantum dot transistors: emission at high charge carrier densities. *Nano Lett* 2015;15:1822–8.
- Yamada K, Yamao T, Hotta S. Light-emitting field-effect transistors having combined organic semiconductor and metal oxide layers. *Adv Mater* 2013;25:2860–6.
- Ullah M, Lin Y-H, Muhieddine K, et al. Hybrid light-emitting transistors based on low-temperature solution-processed metal oxides and a charge-injecting interlayer. *Adv Opt Mater* 2016;4:231–7.
- Walker B, Ullah M, Chae GJ, et al. High mobility solution-processed hybrid light emitting transistors. *Appl Phys Lett* 2014;105:183302.
- Li D, Hu Y, Zhang N, et al. Near-infrared to visible organic upconversion devices based on organic light-emitting field effect transistors. *ACS Appl Mater Interfaces* 2017;9:36103–10.
- Dai X, Zhang Z, Jin Y, et al. Solution-processed, high-performance light-emitting diodes based on quantum dots. *Nature* 2014;515:96–9.
- Anaya M, Rand BP, Holmes RJ, et al. Best practices for measuring emerging light-emitting diode technologies. *Nat Photonics* 2019;13:818–21.
- Kresse G, Joubert D. From ultrasoft pseudopotentials to the projector augmented-wave method. *Phys Rev B* 1999;59:1758–75.
- Bloch PE. Projector augmented-wave method. *Phys Rev B* 1994;50:17953–79.
- Kresse G, Furthmüller J. Efficiency of ab-initio total energy calculations for metals and semiconductors using a plane-wave basis set. *Comput Mater Sci* 1996;6:15–50.
- Kresse G, Furthmüller J. Efficient iterative schemes for ab initio total-energy calculations using a plane-wave basis set. *Phys Rev B* 1996;54:11169–86.

- [47] Kresse G, Hafner J. *Ab initio* molecular dynamics for open-shell transition metals. *Phys Rev B* 1993;48:13115–8.
- [48] Perdew JP, Burke K, Ernzerhof M. Generalized gradient approximation made simple. *Phys Rev Lett* 1996;77:3865–8.
- [49] Li Y, Li Y-L, Sa B, et al. Review of two-dimensional materials for photocatalytic water splitting from a theoretical perspective. *Catal Sci Technol* 2017;7:545–59.
- [50] Dudarev SL, Botton GA, Savrasov SY, et al. Electron-energy-loss spectra and the structural stability of nickel oxide: An LSDA+*U* study. *Phys Rev B* 1998;57:1505–9.
- [51] Miyake T, Zhang P, Cohen ML, et al. Quasiparticle energy of semicore *d* electrons in ZnS: Combined LDA+*U* and GW approach. *Phys Rev B* 2006;74:245213.
- [52] Mashford BS, Stevenson M, Popovic Z, et al. High-efficiency quantum-dot light-emitting devices with enhanced charge injection. *Nat Photonics* 2013;7:407–12.
- [53] Zou Y, Ban M, Cui W, et al. A general solvent selection strategy for solution processed quantum dots targeting high performance light-emitting diode. *Adv Funct Mater* 2017;27:1603325.
- [54] Zhou Y, Fuentes-Hernandez C, Shim J, et al. A universal method to produce low-work function electrodes for organic electronics. *Science* 2012;336:327–32.
- [55] Chen H-C, Lin S-W, Jiang J-M, et al. Solution-processed zinc oxide/polyethylenimine nanocomposites as tunable electron transport layers for highly efficient bulk heterojunction polymer solar cells. *ACS Appl Mater Interfaces* 2015;7:6273–81.
- [56] Shao S, Zheng K, Pullerits T, et al. Enhanced performance of inverted polymer solar cells by using poly (ethylene oxide)-modified ZnO as an electron transport layer. *ACS Appl Mater Interfaces* 2013;5:380–5.
- [57] Choi J, Kim Y, Jo JW, et al. Chloride passivation of ZnO electrodes improves charge extraction in colloidal quantum dot photovoltaics. *Adv Mater* 2017;29:1702350.
- [58] Dong Q, Fang Y, Shao Y, et al. Electron-hole diffusion lengths > 175 μm in solution-grown $\text{CH}_3\text{NH}_3\text{PbI}_3$ single crystals. *Science* 2015;347:967–70.
- [59] Shi D, Adinolfi V, Comin R, et al. Low trap-state density and long carrier diffusion in organolead trihalide perovskite single crystals. *Science* 2015;347:519–22.
- [60] Kim H, Kim JS, Heo J-M, et al. Proton-transfer-induced 3D/2D hybrid perovskites suppress ion migration and reduce luminance overshoot. *Nat Commun* 2020;11:3378.



Lingmei Kong received her M.E. degree in Material Engineering from Shanghai University in 2021. She is currently a Ph.D. candidate at the same university. Her research work focuses on preparation of low dimensional semiconductor nanomaterials and their applications in light-emitting devices.



Feijiu Wang is a full professor of Henan Key Laboratory of Photovoltaic Materials, Henan University, China. His research interest mainly focuses on low dimensional optoelectronic materials and devices.



Xingwei Ding received the Ph.D. degree from Shanghai University, Shanghai, China. His research focuses on semiconductor devices based on metal oxides, in particular oxide thin film transistors.



Xuyong Yang is a full professor at Shanghai University, China. He received his Ph.D. degree in Microelectronics from Nanyang Technological University in Singapore in 2014, and worked as a postdoc at the same university prior to beginning his independent research career at Shanghai University. His research focuses primarily on design and fabrication of low dimensional semiconductor nanomaterials such as quantum dots and perovskite nanocrystals, as well as their applications in light-emitting devices.